Case Studies in Thermal Engineering 37 (2022) 102254

Contents lists available at ScienceDirect

Case Studies in Thermal Engineering

journal homepage: www.elsevier.com/locate/csite

Global fluid flow and heat transfer characteristics analysis of an open air-cooled drive motor for drilling application

Ziyi Xu [a], Yongming Xu [b,*], Wenhui Liu [a,c], Yaodong Wang [d]

[a] School of Electrical and Electronic Engineering, Harbin University of Science and Technology, Harbin, 150080, China
[b] School of Electrical and Information Engineering, Changzhou Institute of Technology, Changzhou, 213032, China
[c] Harbin Electric Corporation, Jiamusi Electric Machine Co., Ltd., Jiamusi, 154000, China
[d] Department of Engineering, Durham University, Durham, DH1 3LE, UK

ARTICLE INFO

Index Terms:
Thermal management
Open air-cooling
Multi-physics coupling analysis
Cooling improvement
Fluid-thermal characteristic

ABSTRACT

The stator winding temperature rise of variable frequency induction motor (VFIM) with high current density may be too high during operation, which properly causes motor breakdowns. Therefore, it is essential to conduct thermal management for VFIM. In this paper, a 600kW VFIM with the open air-cooling is studied at the point of thermal. A compact cooling improvement structure, axial ventilation guide vane, is proposed to strengthen the heat dissipation capacity of the motor. The global numerical model based on the multi-physics bidirectional coupling method is established to provide a comprehensive understanding of fluid-thermal characteristics in the motor. Based on simulation results, the cooling improvement is analyzed and discussed from multiple perspectives, such as temperature, flow, vortex, etc. It is concluded that the proposed structure can reduce the maximum and average temperature rise of the stator winding by 1.4K and 0.7K, respectively. Moreover, the effect of installation location on the cooling effect is investigated. When the proposed structure is installed on both sides, the overall heat dissipation power rises to 42299.7W. The experiment was also conducted to verify the simulation results. The relative error between simulation results and experimental data is 4.4%.

1. Introduction

In the intensely competitive petroleum market, the demand for high-performance and inexpensive solutions indicates the need for drives with high torque or power density. It means that as well as designing scheme improvements with the purpose of enhancing compactness and output capacity, the drive motor should be operated at the electromagnetic limit and thermal limitation to make full use of materials. Therefore, accurate evaluations of electromagnetic performance and temperature distribution of the motor during operation in the design stage are essential for the maximum possible utilization of the motor. Research on electromagnetic and thermal analysis for high-performance motors has become a hot issue. However, a review of scientific literature during the past few years indicates a lopsided degree of development among electromagnetic and thermal analyses of motors.

When the drive motor for drilling applications operates at their electromagnetic limit, a significant amount of losses are generated inside them. Most losses generated are converted into heat, which leads to a high temperature rise in the main components of the motor. Excessive temperature rise will increase the speed of motor life consumption and the possibility of failure. Thus, accurate thermal analysis and effective cooling design of the motor are of exceptional importance as they can ensure the long-term stable

* Corresponding author.
E-mail address: xuyongming@czu.cn (Y. Xu).

https://doi.org/10.1016/j.csite.2022.102254
Received 2 May 2022; Received in revised form 17 June 2022; Accepted 28 June 2022
Available online 30 June 2022

operation of the motor.

Computational fluid dynamics (CFD) is a pretty powerful and effective tool capable of obtaining a detailed and precise fluid field and temperature field distribution of the motor with a complex geometric structure [1–3]. Furthermore, CFD can also provide insightful and perceptive opinions on improving heat dissipation [4–7]. The thermal behavior of a motor not only depends on its cooling capacity but also has a lot to do with electromagnetic losses. Main electromagnetic losses generated during operation vary with temperature, mainly because the resistivity of materials increases with temperature. To simulate the physical phenomena in the motor more realistically and achieve a higher-precision simulation, the multi-physics coupling analysis method is more and more frequently applied to thermal analysis [8,9]. The most crucial physical fields from the thermal management point of perspective are the field of electromagnetic, temperature, and fluid, and temperature is the key to the coupling of the three physical fields. Electromagnetic losses and physical properties of materials are functions of the temperature as the independent variable, and coupling parameters among different physical fields. The coupling analysis process may be unidirectional or bidirectional [10,11]. The latter can achieve a more accurate simulation but is also much more demanding in terms of computational cost. Moreover, due to the uneven distribution of electromagnetic losses, the transmission of loss data between different physical field calculation models is also an important issue [12,13]. Without proper application of the loss mapping method, continuation in improving the accuracy will not be possible. Although some studies have been conducted based on coupling analysis, there are more or less deficiencies in coupling parameters, loss mapping, and coupling ways.

Because the rotation of the rotor restricts the application of many effective cooling methods, how to effectively enhance the heat dissipation of the rotor has always been a hot topic for research for those interested in motor thermal management. In recent years, many investigations have been conducted to provide the essential understanding of cooling the rotor by hollow shaft cooling [14–16] and related cooling methods derived from it [17,18]. However, the additional equipment required for cooling, such as pumps, oil tanks, and heat exchangers, will reduce the reliability and cost-effectiveness of the motor. It limits the application on some special occasions. Traditional forced air cooling has the advantages of high reliability and low price. A properly designed and arranged fan can ensure that the rotor temperature is within a reasonable range [19,20]. Nevertheless, the introduction of fans will increase the axial length of the motor, which will lead to a negative effect on the enhancement of power density. It is the case for the machine presented in this article, which has high electric density and requires high reliability and compactness.

In light of the aforementioned, this paper proposes a multi-physics bidirectional coupling analysis method with more careful considerations and a novelly innovative heat dissipation enhanced structure, called axial ventilation guide vane (AVGV). The proposed structure can enhance the heat dissipation capability without increasing the volume of the motor. Besides, the proposed structure is cost-efficient and can be applied to the existing motor design scheme.

The rest of this paper is arranged as follows. Firstly, the methodology is detailedly described, including the parameters and ventilation structure of the motor, proposed cooling structure and simulation method, and experimental platform. Then, the temperature field results of the motor are discussed in detail and depth, and the accuracy of simulation results is verified by experiments. Finally, the cooling capability of AVGV is analyzed from multiple perspectives.

2. Characterization/description of the open air-cooled drive motor

A. Prototype Parameters

YYZ600/600–01, a variable frequency three-phase induction motor, is the research object in this paper. The use of open slots and rectangular conductor windings together enables the motor to achieve a relatively high slot fill factor. To reduce harmonic currents, the air gap of the motor is slightly larger than that of the motor of the same specification. The motor is designed with a high electromagnetic load to meet the requirements of application scenarios. Furthermore, the overall structure of the motor is compact, especially in the axial direction. Table I lists the basic parameters making up the prototype.

B. Cooling Configuration and Improvement Scheme

The cooling mode of the motor is open forced air-cooling, and the schematic diagram of the air circulation path in it is shown in Fig. 1(a). A ventilator with an air supply volume of 110 m^3/min is installed on the upper part of the housing at the non-drive end (NDE) side. It draws the external cold air into the end air domain of the NDE side. Then, the air flows into the iron core domain under pressure.

Table 1
Prototype basic parameters.

Name	Value
Rated power (kW)	600
Rated voltage (V)	600
Number of poles	6
Frequency (Hz)	33.5
Insulation grade	H
Core length (mm)	536
Air gap thickness (mm)	1.8
Number of stator/rotor slots	72/62
Stator winding current density (A/mm^2)	5.72
Rotor conductor current density (A/mm^2)	5.33

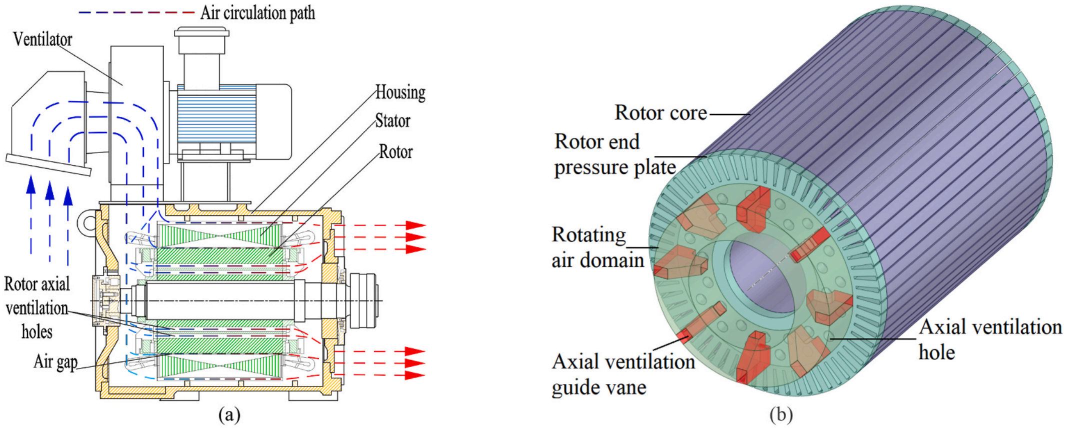

Fig. 1. Cooling arrangement. (a) Air circulation path. (b) Cooling improvement scheme.

There are three axial paths for the air in the iron core domain. The first is located between the housing and stator core with a height of 10 mm, the second is the air gap, and the third is located at the rotor core yoke. A total of 32 axial ventilation holes (AVH) with a diameter of 20 mm are provided on the rotor core yoke. These holes are divided into two layers in the radial direction, with 16 evenly distributed in each layer. Besides, the ventilation holes corresponding to the upper and lower layers differ by 11.25° in the circumferential direction. There are four outlets on the end face of the housing on the DE side, and the cold air finally flows out from these four outlets after absorbing the heats.

In a forced air-cooled motor, built-in coaxial axial or centrifugal fans are usually used to enhance air pressure to allow air to pass through the motor. However, for the motor in this paper, the role of the fan is redundant because the ventilator has raised the pressure of air to a sufficient level. Unlike fans, AVGV aims to match the airflow trajectory with the motor's internal geometry to improve the airflow condition. Due to the limitations of the application, the motor axial structure is required to be compact. Moreover, AVGV needs to rotate like a fan to play its role. Therefore, the specific scheme is to install AVGV on the rotor end pressure plate by welding, and the schematic diagram of the cooling improvement scheme is shown in Fig. 1(b). In this way, the axial length of the motor will also not increase due to the relatively small geometry of AVGV.

AVGV rotates with the rotor and exerts a normal force perpendicular to the shaft to the surrounding air (the rotating air domain in Fig. 1(b)). Under the action of force, the surrounding air will generate a normal velocity component. After being combined with the original velocity vector, the angle between the new velocity vector and the axial direction will increase. The amount of air flowing out of axial ventilation holes and directly hitting the end cover on the DE side will be reduced, and the reduced portion will flow toward the outlet. The flow behavior in the end air domain of the DE side will be improved, which is beneficial to heat dissipation.

This paper will perform analyses and discussions on the following four cases: (a) the motor with no AVGV, (b) the motor with AVGV on the NDE side, (c) the motor with AVGV on the DE side, (d) the motor with AVGV on both side. And case a is used as the original case in the discussion and analysis of Section V.

3. Numerical analysis methodology

The motor in this paper is specially designed as the drive motor for the electric drive drilling rig. It is the crucial equipment directly related to drilling efficiency and success rate. It means that the reliability of the motor should reach a very high level. Research has shown that temperature is the main factor affecting the reliability of the motor [21]. Therefore, accurate thermal analysis is essential as

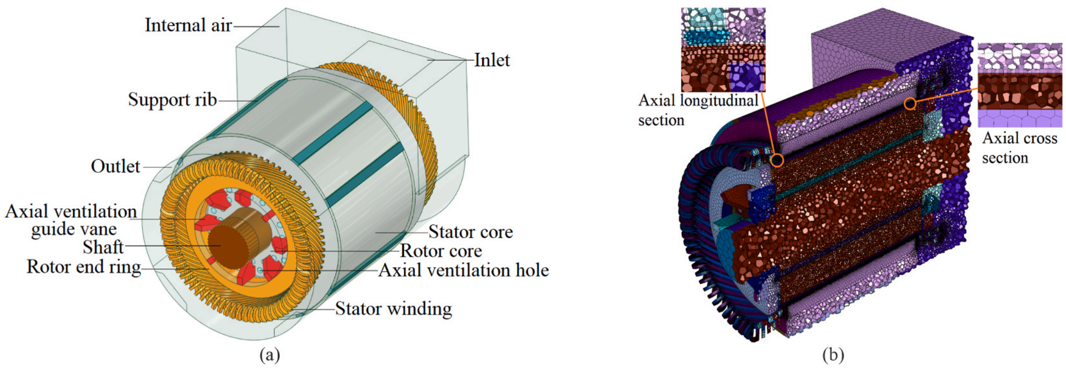

Fig. 2. CFD analysis. (a) Physical model. (b) Detail of the 3-D mesh.

it can ensure a reliable long-term operation.

A. Loss analysis

Various losses within the motor are regarded as the area distributed heat source to conduct a thermal analysis. Therefore, accurate loss characteristics estimation is the prerequisite for a reliable thermal analysis. The distribution and magnitude of electromagnetic losses, including copper and iron losses, are estimated by 2-D finite element analysis (FEA), which can reduce the calculation cost as much as possible while ensuring the high accuracy of results. Stray load losses and mechanical losses are measured through experiments. Moreover, stray load losses are distributed according to the improved formula proposed in the literature [22].

B. Fluid and Thermal Analysis

To investigate the steady-state fluid and thermal characteristics of the motor, a 3-D CFD analysis model is established and solved. The physical model includes the whole air domain inside the motor housing (iron core and end domain) and major structures of the motor, as shown in Fig. 2(a).

Since the ventilator is closely connected to the housing, it is believed that all the cold air driven by it enters inside the motor without leakage. Therefore, the ventilator is not involved in the physical model. For the motor studied in this paper, the end air domain is one of the main areas for heat exchange. To accurately simulate the fluid motion and heat exchange behavior in this domain, geometric features of the end winding are entirely reproduced in the physical model. Only a minimal amount of heat is transferred to the housing because of the air duct between the stator core and housing. Therefore, the housing is not involved. It is replaced with walls with a constant temperature in the simulation. The stepped shaft is simplified into a cylinder with a constant diameter. And the tiny geometric features, such as chamfering, which have no or a minor effect on fluid flow and heat transfer, are also simplified. For the winding, the copper in it is merged into a single body. Shell conduction can be employed to simulate one or more layers of thin-wall cells without the demand to discretize the thin wall in pre-processing. So it is utilized to model the heat transfer of the insulation, such as slot insulation/liner and impregnation. With the simplifications mentioned above, the physical model is simplified considerably without diminishing the accuracy of the analysis.

Table II lists the thermal properties of materials used in the simulation. The thermal properties of air are defined as changing with temperature, including dynamic viscosity, specific heat capacity, thermal conductivity, and density.

A detail of the mesh discretization is shown in Fig. 2(b). Compared to tetrahedral meshes, polyhedral meshes can provide a fine discretization scheme with a low total amount and high quality due to the superiority of the grid amount control, convergence performance, and flexibility [23]. The entire solution domain is finely discretized with the polyhedral mesh, and meshes of the regions with a significant gradient or minor geometric feature have been refined, such as the air gap and end winding. The total number of grids is 15286806. The maximum, minimum, and average skewness of grids are 7.6×10^{-1}, 1.6×10^{-3}, and 8.2×10^{-2}, respectively, which indicates that the grids created are with a low degree of skewness, characteristic of the high-quality grids. Moreover, the conformal mesh is applied between different unit zones to realize a high precision computation.

The rotational motion is simulated through the Multiple Reference Frame (MRF), which is more proper for steady-state research and less computationally cost with respect to the Sliding Mesh. The turbulence model employed in this investigation is the SST k-ω. The dimensionless number Br, Brinkman number, is used to describe the effect of viscous heating and is expressed as follow:

$$B_r = \frac{\mu U_e^2}{k\Delta T} \tag{1}$$

where μ is the absolute viscosity of the fluid, U_e is flow velocity, k is thermal conductivity, and ΔT is the temperature difference. By calculation, $Br > 1$, viscous heating needs to be considered in the analysis. Finally, the simulation is conducted on a Lenovo workstation with 2 × Intel Xeon E5-2650 v4 and 256 GB DDR4 memory.

C. Multi-physics Coupling Analysis Method

Different natures of physical fields in the motor have a close interaction. When the motor is operating, most of the losses generated are converted into heat, making the temperature of the substance in the motor rise. Temperature changes will affect the conduction properties of electromagnetic materials and the thermophysical properties of the cooling medium [24,25]. As a result, the loss characteristics of the motor and the overall heat dissipation capacity will change accordingly, which will lead to a new temperature distribution. Therefore, considering interactions among different physical fields is much essential for a precise thermal analysis. The typical method for multi-physics coupling analysis only consists of one iterative loop. It means that the physical fields considered in the analysis need to be solved in each iteration, which is very expending in computational time.

In this paper, a coupled analysis method with double circulation loops is proposed. The flowchart is shown in Fig. 3. The analysis

Table 2
Thermal properties of materials.

Part	Thermal conductivity W/m·K	Density kg/m^3	Specific heat capacity J/kg·K
Conductor	387.6	8979	381
Iron core	$k_x = k_y = 40$, $k_z = 2$	7800	460
Insulation	0.26	930	1340
Shaft	40	8030	502.48

process consists of an inner circulation and an outer circulation. The inner circulation only analyzes the fluid-thermal characteristics of the motor, while the electromagnetic field analysis is included in the outer circulation. When the initial temperature T_0 (the ambient temperature measured from experiments) is given, the electromagnetic analysis is first performed. Its result is used as the heat source for the flow-thermal analysis. When transferring to the inner circulation calculation, only the thermophysical properties of materials are updated in each iteration. After the inner circulation converges, the outer circulation convergence condition is judged. If it does not, material conduction characteristics are updated according to the temperature results. The outer circulation is performed again to calculate the heat source, and results are transferred to the inner circulation. Through this flow process design, the times of electromagnetic analysis needed to be solved and data mappings are reduced. The simulation solution time can be effectively reduced.

4. Experimental platform

Experiments are conducted to determine required losses and verify the accuracy of simulation results. The general name of the experimental platform is called the electrical test station power supply and distribution and digital operating system, which can measure the electrical parameters, output capacity, and temperature of the motor. Electromagnetic parameters of the original and improved motor are the same. The only difference between the two is whether AVGV is employed. Considering the temperature rise results of each major part of the motor and the rotor dynamic balance, the improved motor of case d is taken as the prototype to be manufactured and tested.

The no-load and rated load experiments are performed. Experimental methods and operations strictly comply with GB/T 1032. The procedures of the experiment are shown in Fig. 4(a). The required losses can be obtained by processing simulation results and experimental data. Besides, the ambient temperature is also measured in the experiment.

The motor shaft does not carry any mechanical load during the no-load experiment. When the change of motor input power is less than 3% within 30 min, the motor is considered to reach a no-load steady-state, and the input power is recorded. The recorded no-load input power is the total no-load loss of the motor. Mechanical losses can be obtained by subtracting the copper and iron losses estimated by no-load FEA analysis from the total no-load losses measured in the no-load experiment.

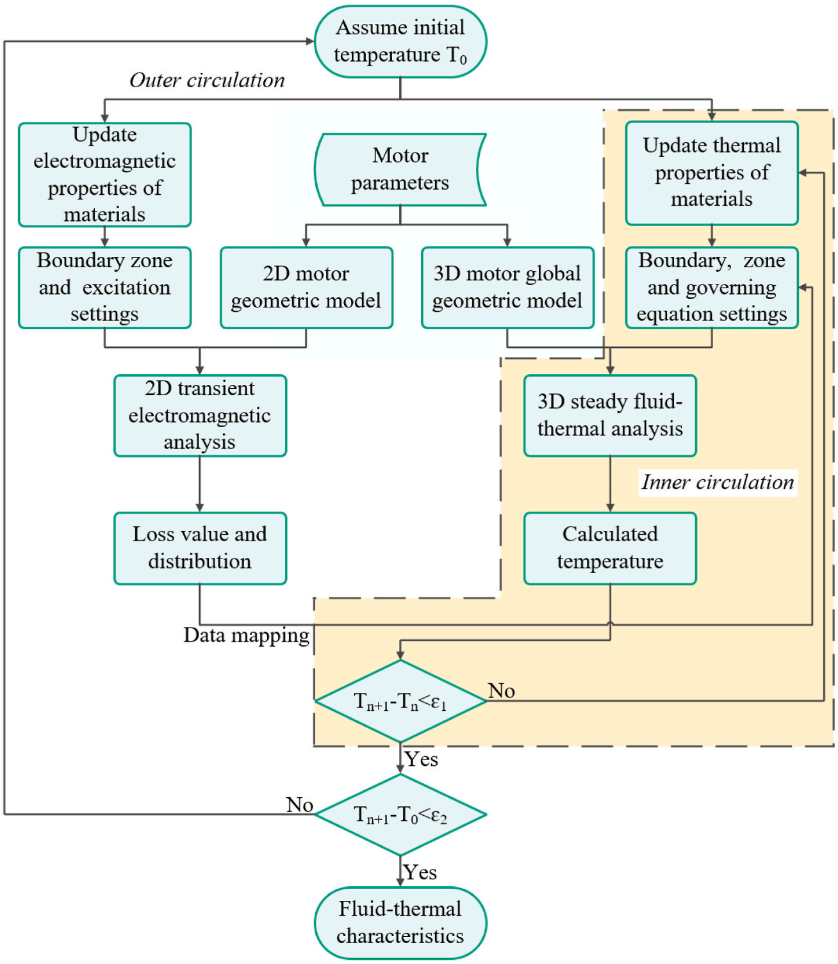

Fig. 3. Flowchart of multi-physics coupling analysis.

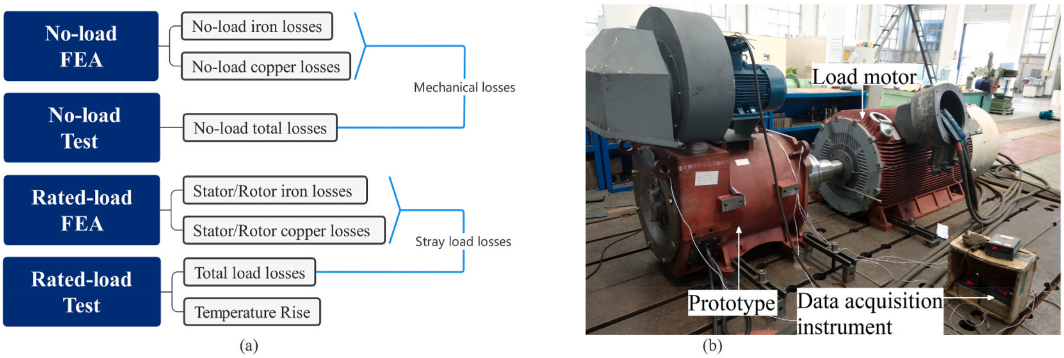

Fig. 4. Experiment. (a) Diagram for the characterization of the loss and temperature. (b) Motor drag experiment.

The load experiment is the motor drag experiment in which a motor with appropriate power works in the generator state as the load of the prototype, as shown in Fig. 4(b). The temperature is measured by Pt100. There are twelve sensors in total (two in each slot, one for use and the other for backup), which are evenly buried in the circumferential direction and located between the double-layer windings. When the temperature change is less than 0.5K in 30 min, the motor is considered to reach the thermal steady state. Input power, output power, and temperature measurement sensor data are recorded. The difference between the two power data is the total loss under the load. Stray load losses are determined by subtracting losses estimated by rated-load FEA analysis and mechanical losses from the total load losses measured in the rated-load experiment.

Through data processing, mechanical losses and stray load losses are 348.9W and 7081.6W, respectively. The ambient temperature is 35 °C, which is used as the initial temperature for analysis. The measured temperature data will be compared and analyzed with simulation results in the later section.

5. Results and discussion

A. Temperature Characteristics Results Analysis

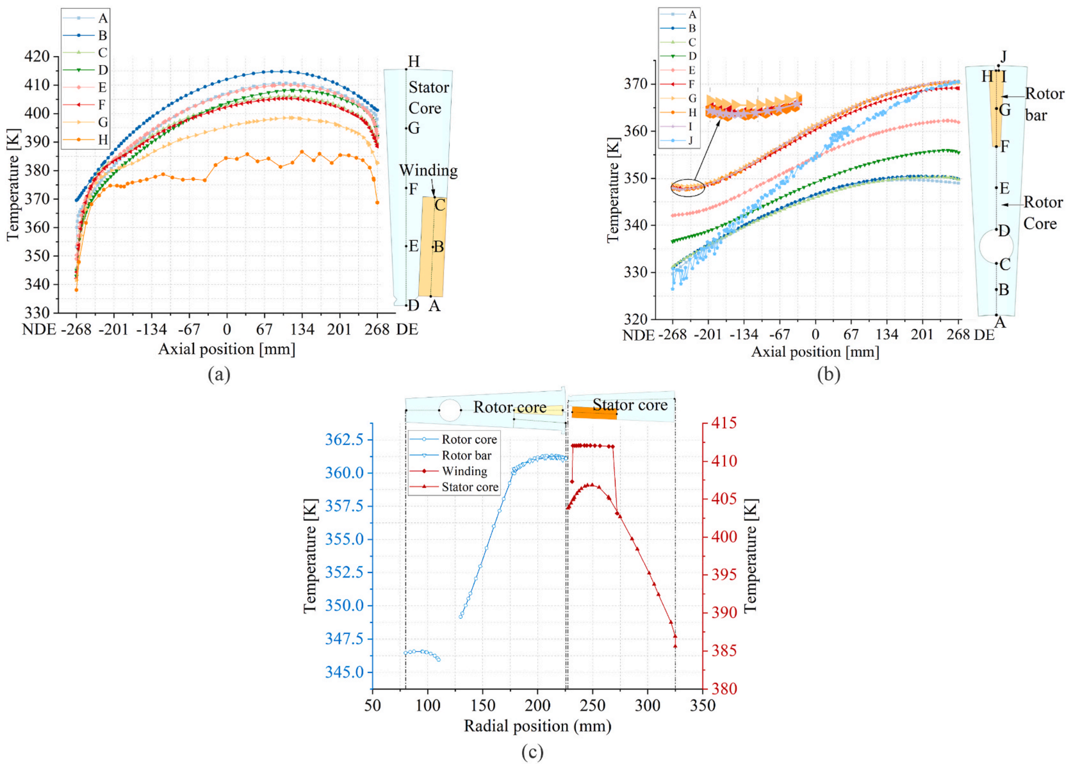

Fig. 5. Temperature variations curve. (a) Stator region along the axial direction. (b) Rotor region along the axial direction. (c) Primary structures at z = 0 mm along the radial direction.

The temperature variations of primary structures in the iron core zone are shown in Fig. 5. The horizontal coordinate in Fig. 5(a) and (b) from −268mm to 268 mm is from the core end face on the NDE side to the core end face on the DE side, and the same is true in the latter figure.

It can be seen from Fig. 5(a) that the temperature increases initially and then drops along the axial direction. The peak value is reached at the axial middle near the DE side. For the studied motor, stator end windings are surrounded by the cold air with a high flow velocity and are also with a broad convective heat transfer area. Losses generated in the end windings can be dissipated in time and will not be transmitted to the in-slot part. In contrast, in-slot windings are surrounded by the iron core and slot wedge, making the thermal resistance between them and cold air greater than that of end windings. Although losses generated in the end winding are slightly higher than the in-slot winding, the hot spot is in the middle of the winding. In addition, the stator outer surface temperature (point H) is mainly affected by the fluid flow characteristics around it, and the air between the housing and stator core is in a turbulent state. Therefore, the curve has a large fluctuation.

For the rotor region, the distribution rule is different from the stator region, as shown in Fig. 5(b). The temperature gradually rises along the axial direction, which is mainly attributable to the difference in the heat dissipation condition of the dominating heat source. On the one hand, the heat dissipation area of the rotor conductor in the end region is much smaller than that of the stator winding. On the other hand, the open slot design and no insulation provide a fine heat dissipation condition for the in-slot rotor conductor. The difference in thermal resistance from the in-slot and end conductor to the cold air is relatively small. Therefore, the temperature distribution in the rotor region varies with the cooling gas temperature.

From the enlarged view in Fig. 5(b), it can be seen that there is a slight temperature drop of points F, G, H, and I around $z = -248$mm. It is due to the sudden contraction of the cross-sectional area of the flow path, which creates vortices near the wall at the entrance of the air gap, resulting in weakened convective heat transfer. Therefore, the temperature of the rotor core and conductor at the entrance of the air gap is slightly higher than the adjacent area. In addition, the situation of point J in the rotor region is similar to that of point H in the stator region.

Fig. 5(c) shows the temperature variation of primary structures at $z = 0$ mm along the radial direction. The radial temperature gradient is much small in most areas of the stator winding but is considerable at the radial edge. The reason is that the thermal conductivity of the insulation is much small, which is several orders smaller than that of the copper. It results in a sudden sharp

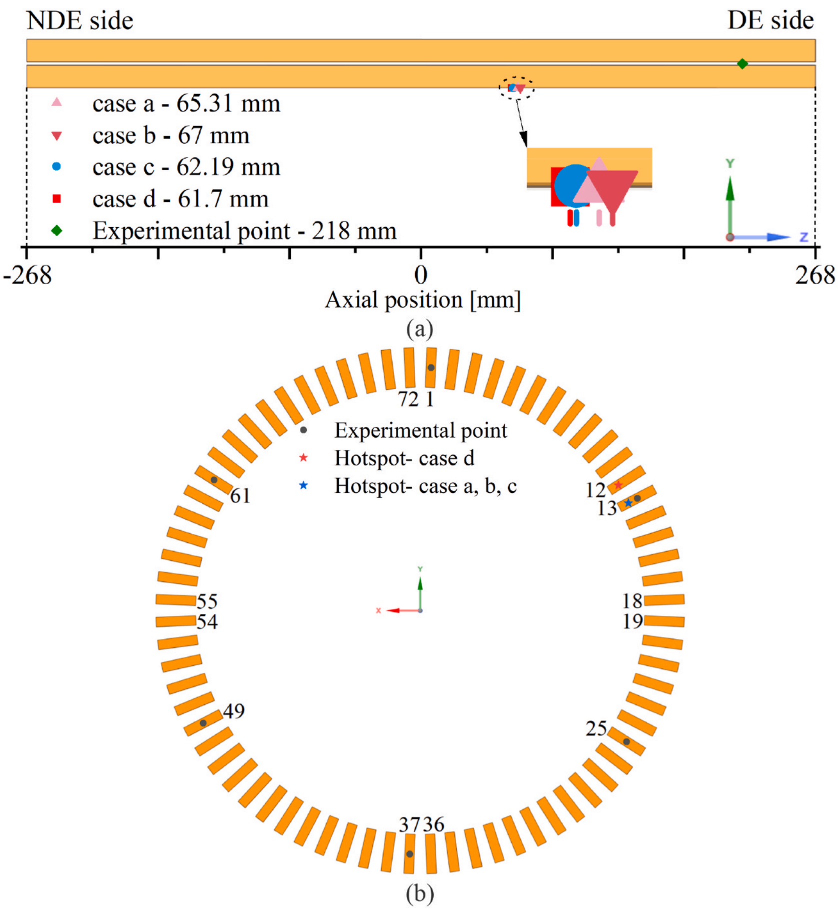

Fig. 6. The position of the hotspot and experimental point. (a) Axial. (b) Circumferential and radial.

weakness in heat conduction. As for the stator core, the high-temperature area is mainly concentrated at the stator teeth. The contact area between the stator winding and the stator teeth is larger than that with the stator yoke, so a considerable part of copper losses is transmitted to the stator teeth. Furthermore, the core loss of the stator teeth is also higher than that of the yoke.

Similar to the stator region, the radial temperature distribution of the rotor region is also radiated from the main heat source (rotor bar) to the radial ends. The temperature of the rotor bar at the radial middle is slightly higher than that at both radial sides. For the rotor core, the region with the same radial position as the rotor bar, the radially outer region, has the same distribution rule as the rotor bar. In the radial middle region, with the increase of the distance from the rotor bar, the temperature gradually decreases, and the temperature gradient of this region is larger than that of the radially outer region. The employment of axial ventilation holes can effectively prevent rotor copper losses from transferring to the radially inner region. Moreover, only very little loss generates in the radially inner region and shaft. Therefore, there is a temperature drop between the radially inner region and the other two regions.

The temperature distribution and variation law of the other three cases are the same as case a. The differences between different cases are the specific location and value of the hotspot, as well as the magnitude of the average temperature, etc.

The specific locations of the hotspot for each case and experimental measurement points are shown in Fig. 6. For all four cases, the hotspot of the motor is located at the in-slot stator winding. On the one hand, from the perspective of the axial position, case a, as the reference case, is located at z = 65.31 mm, 62.18% of the axial position of the iron core domain. The introduction of AVGV on one side enhances the convective heat transfer intensity in the corresponding end region so that the hotspot moves to the other side. The hotspot of case b and case c moves to z = 67 mm and z = 62.19 mm, respectively. Compared with case a, the hotspot of case d moves 3.61 mm to the NDE side, and the moving distance is the largest among the three cases, indicating that the enhancement of the heat dissipation capacity of the DE side is significantly higher than that of the NDE side in this situation.

On the other hand, from the perspective of the circumferential and radial position, the hotspot of cases a, b, and c are all located at the center of the lower winding of the 13th slot, while case d is located at the same radial position of the 12th slot. Limited by the ventilator, the inlet is located directly above slots 55 to 72. The cold air directly hits the end windings of slots 55 to 72 after entering the motor, then flows to the lower half of the motor, and finally circulates to the region of slots 1 to 18. Therefore, the air through the region of slots 1 to 18 is few, and the temperature is higher because the cooling gas has absorbed winding losses in other regions.

Table III lists the maximum and average temperature rise of primary structures for each case. The stator winding of cases b and d have the lowest temperature rise of 118.8K. However, the average temperature rise of case b is lower than case d. Compared with case a, the maximum temperature rise and average temperature rise of the stator winding decrease by 1.4K and 0.7K at most, and the decreases are about 1.2% and 0.8%. Case c has the lowest temperature rise of the rotor region. Compared to case a, the reduction in maximum and average temperature rise of the rotor region is between 0.4% and 1.3%.

As can also be seen from Table III, when AVGV is only installed on the NDE side, the temperature rise of the stator region is the lowest. When only installed on the DE side, the temperature rise of the rotor region is the lowest. When installed on the both sides, the temperature rise of both stator and rotor regions is reduced. Case d has a good overall cooling. However, focused on a single region, the reduction is smaller than that in the case of single-side installation.

Since the exact position of Pt100 cannot be determined, a line segment parallel to the plane of the slot bottom is taken at the corresponding axial position between the upper and lower windings. The temperature range corresponding to the line segment is used as the simulation result. The comparison between simulation results and experimental data is shown in Fig. 7. The temperature rise measured in the experiment is 98.48K, which is the average of 6 temperature measurement points. The maximum error between simulation results and experimental data is 9.27K at slot 25, and the maximum relative error is 9.4%. The error between the experimental data and the average of simulation results is 4.32K, and the relative error is 4.4%. It shows that the established simulation model is in line with the actual condition, and the precision and credibility of the proposed calculation method and the simulated results are validated.

As can also be seen from Fig. 7, only the temperature range of slots 1 and 61 contains 98.48K, while the minimum value of the simulation results of the remaining slots are all greater than 98.48K. Overall, simulated results are higher than the experimental data. It is because the temperature rise measured experimentally is the insulation temperature rise. However, the winding is simplified for a quick simulation, so the temperature range corresponding to the line segment mainly represents the temperature rise of the copper.

B. Flow Characteristics Results Analysis

The variation curve of the fluid velocity along the axial direction is shown in Fig. 8(a). The fluid velocity between the stator core and housing is the highest, followed by the AVH and the lowest in the air gap. Moreover, the fluid velocity in the air gap is about half of the other two paths. For pipe flow and concentric cylinder flow, the flow velocity of the mainstream fluid mainly depends on the flow

Table 3
Maximum and average temperature rise of different cases (K).

	Stator				Rotor			
	Winding		Core		Conductor		Core	
	Max	Ave	Max	Ave	Max	Ave	Max	Ave
a	120.2	88.2	116.4	90.4	63.0	52.6	63.3	46.0
b	118.8	87.5	115.2	89.2	63.1	52.7	63.3	46.3
c	119.3	88.0	115.6	90.1	62.3	52.2	62.5	45.8
d	118.8	88.1	115.2	90.1	62.8	52.6	63.1	46.0

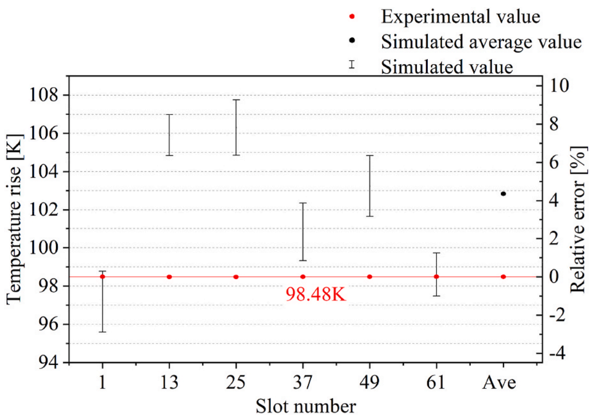

Fig. 7. Comparison of the temperature rise obtained from the experiment and simulation.

rate and the cross-sectional area of the flow path. Although the cross-sectional area of the air gap is much smaller than the other two flow paths, there is less air flowing through it than in the other two.

It can also be seen that the fluid velocity in the lower half of the motor is slightly higher than that in the upper half. It means that after entering the motor, more air flows through the lower half of the motor. This may be considered a further illustration of the location of the hotspot. Besides, the velocity increases sharply near the inlet after the fluid just enters the air duct between the stator core and housing and AVH. It is due to the sudden shrinkage of the flow path. Compared to the air duct between the stator core and housing, the sharp increase in velocity at the AVH inlet is significantly larger due to a greater shrinkage ratio. After the flow is fully developed, the fluid velocity gradually stabilizes.

Fig. 8(b) shows the fluid mass flow distribution of different cases. The total mass flow rate at the inlet is 2.246 kg/s. About 65% of the air flows through the air duct between the stator core and housing, ensuring that the stator region with a high loss density is within a reasonable temperature range. About 30% of the air flows through AVH, which can effectively dissipate the heat generated by rotor bars to avoid heat transfer to the shaft, thereby affecting the service life of the bearing. Only about 5% of the air flows through the air gap, so the fluid velocity is relatively low.

AVGV functions like a centrifugal fan, which can change airflow direction near itself. However, due to the employment of AVH and the limitation of vanes geometric parameters, the ability to deflect air is not as strong as centrifugal fans. As can also be seen from Fig. 8 (a), When AVGV is introduced, the air flowing through the stator region slightly increases. The temperature rise of the stator region decreases accordingly. This conclusion holds for cases b, c, and d. For the rotor region, the application of AVGV results in less air flowing through this region. However, the changes in temperature rise are not the same for different cases. Case c has the lowest temperature rise of the rotor region, while case b is the highest and even worse than case a.

For case d, the amount of air flowing through the air gap increases significantly, by up to 8% compared to case a. The reason is that the distribution of the reduced airflow from AVH changes. About 70% is transferred to the air gap, and only about 30% is transferred to the air duct between the stator core and housing. The air flowing through the air gap cools both the stator and rotor core, thus achieving a good overall cooling instead of a single region.

Fig. 9 shows the fluid velocity vector distribution in the end region of the DE side. It can be seen that after the air between the stator and housing flows into this region, only a small part directly flows to the outlet. Most of the air (emphasized with the black circle) flows

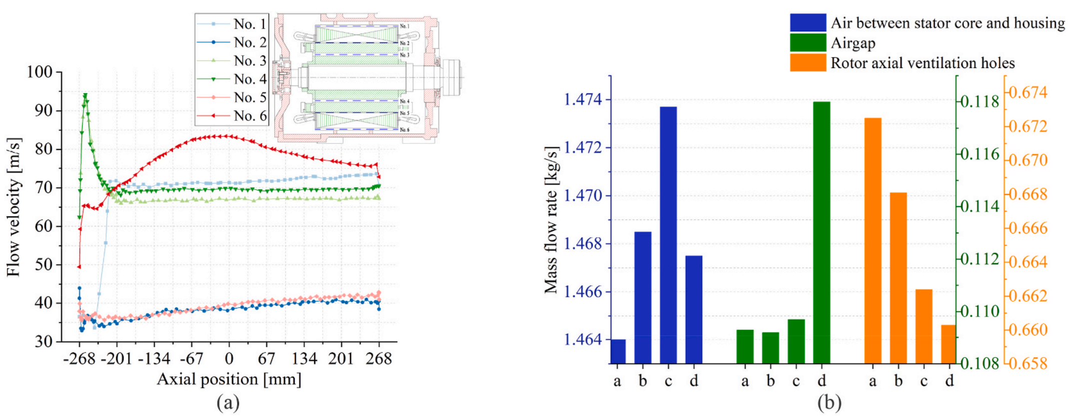

Fig. 8. Flow Characteristics. (a) Fluid velocity variations in the main flow path along the axial direction. (b) Fluid mass flow rate distribution of different cases.

along the inner wall of the housing to the area near the rotor end face and collides with the air flowing from AVH, which results in many vortices. When AVGV is applied on the DE side, a part of the air flowing from AVH flows to the stator region under its action. The amount of collision gas and vortices is effectively reduced. As a result, the flow resistance of the end region decreases.

Q criterion is an important calculation to identify vortices, defined as follow:

$$Q = 0.5^*\left(\| B\|_F^2 - \| A\|_F^2\right) \tag{2}$$

$$A = 0.5^*\left(\Delta V + \Delta V^T\right) \tag{3}$$

$$B = 0.5^*\left(\Delta V - \Delta V^T\right) \tag{4}$$

where A, B are the symmetric and antisymmetric tensors of velocity gradient, respectively, T represents the transpose of the matrix. Q criterion normalized volume rendering of the end region of the DE side is shown in Fig. 10. After AVGV is introduced on the DE side, the region where the Q criterion normalized is greater than 0 is significantly reduced, which indicates a reduction in vortices, validating the previous analysis. In addition, taken temperature characteristics results together, it can be found that the temperature rise of the rotor region is more influenced by the fluid flow conditions in the end region of the DE side.

C. Heat dissipation analysis

The surface average heat transfer coefficient is an important index for evaluation of convective heat transfer intensity, given as follow:

$$\overline{h_i} = \frac{1}{A_i}\int_{A_i}\frac{q_i(x,y,z)}{A_i(T_{wi} - T_\infty)(x,y,z)}dA_i \tag{5}$$

where q_i is the heat flow through surface A_i, T_{wi} is the surface temperature of surface A_i, T_∞ is the bulk fluid temperature.

Table IV lists the surface average heat transfer coefficients of different cases. When AVGV is applied on the NED side, the surface average heat transfer coefficient of each surface of the stator region increases except for the inner surface of the stator core. And case b has the highest average heat transfer coefficient of the stator winding surface among the four cases. However, only from the point of view of the surface average heat transfer coefficient, case c which the temperature rise of the rotor region is the lowest, cannot be reasonably explained. It is because the size of the surface heat transfer coefficient reflects the strength of convective heat transfer but does not represent the surface heat dissipation power. There are other factors that affect the surface heat dissipation power, such as the flow state of the fluid and the geometric factors of the heat exchange surface.

Table V lists the surface heat dissipation power of different cases. By analyzing the data in the table, it can be obtained that the sum of the surface heat dissipation power of the stator region of case b is the largest, which is 30367W. A similar conclusion for the rotor region of case c can also be obtained. The sum of the surface heat dissipation power of the rotor region of case c is the largest among the four cases, at 11948.4W. In contrast, the overall surface heat dissipation power of case d is the largest of all cases at 42299.7W. It can be considered a further validation of the temperature characteristics results.

6. Conclusion

This paper addressed the thermal management for an open air-cooled drive motor with high current density used in drilling. With the aim of obtaining a comprehensive and accurate understanding of fluid-thermal characteristics of the motor and strengthening

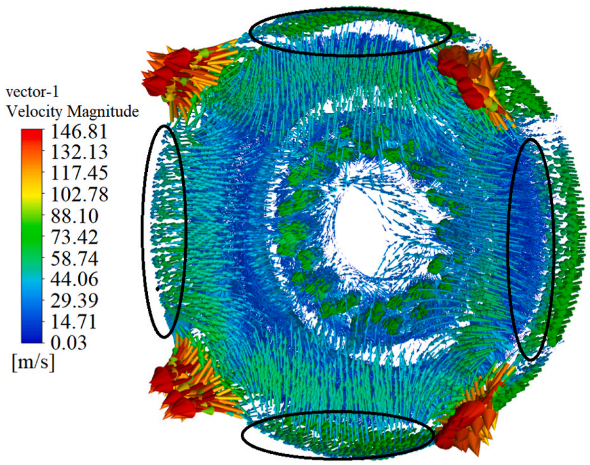

Fig. 9. Fluid velocity vector distribution at end region of the DE side.

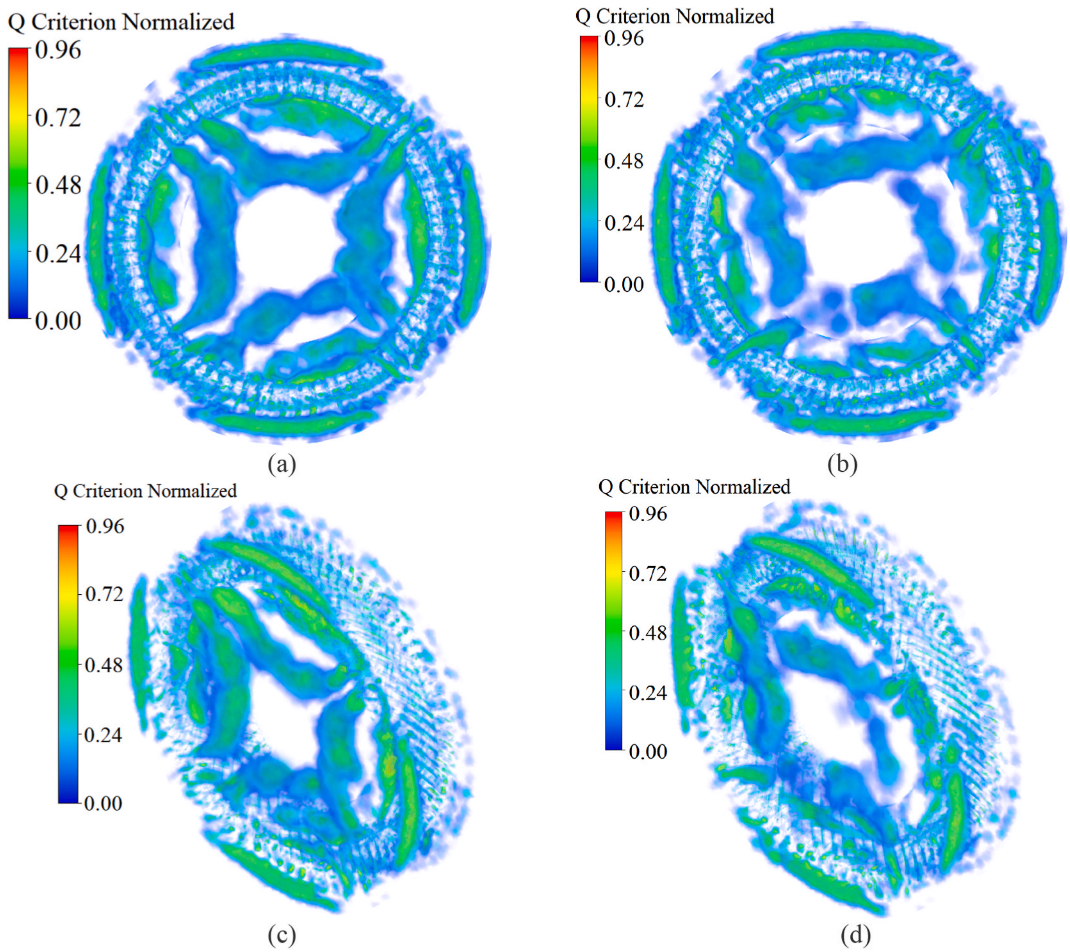

Fig. 10. Volume rendering of *Q* Criterion normalized. (a) +Z view of case a. (b) +Z view of case c. (c) Isometric view of case a. (d) Isometric view of case c.

Table 4
Surface average heat transfer coefficient of the different cases ($W/m^2 \cdot K$).

	a	b	c	d
Stator core outer surface	140.3	140.7	140.6	141.0
Stator core inner surface	59.0	58.0	59.3	58.5
Stator core NDE surface	85.7	87.1	85.8	87.1
Stator core DE surface	19.6	20.8	20.6	20.0
Stator winding NDE surface	71.6	72.1	71.8	72.0
Stator winding DE surface	54.4	55.1	53.5	52.7
Rotor core outer surface	27.8	27.0	27.8	27.2
Rotor AVH surface	96.2	94.8	95.6	94.9
Rotor core NDE surface	67.0	65.6	66.7	66.2
Rotor core DE surface	41.9	41.7	39.4	37.7
Rotor bar surface	46.7	44.6	47.0	50.1
Rotor end ring NDE surface	70.8	69.5	71.3	69.2
Rotor end ring DE surface	66.5	68.5	62.5	61.8
Shaft surface	46.3	47.8	44.5	46.3

motor heat dissipation capability, a multi-physics bidirectional coupling analysis method with more careful considerations and a cooling improvement structure were proposed. Experiments were performed to verify the accuracy of the proposed method. The maximum relative error between the simulation results and experimental data was 9.4%, and the average relative error was 4.4%, which proves the accuracy of the simulation results.

The proposed structure, AVGV, can reduce the magnitude of motor hotspot temperature rise. When AVGV is installed only on the NDE side, it is beneficial to reduce the temperature rise of the stator region and increase the air flowing through it. The maximum temperature rise of the stator winding decreases by 1.2%. When only installed on the DE side, the temperature rise of the rotor region is

Table 5
Surface heat dissipation power (W).

	a	b	c	d
Stator core outer surface	12865.6	12856.8	12849.8	12910.9
Stator core inner surface	4466.1	4413.7	4483.1	4458.9
Stator core end surface	1205.7	1228.3	1215.3	1222.1
Stator winding NDE surface	6005.7	6035.7	6023.8	6028.2
Stator winding DE surface	5777.2	5832.5	5774.3	5744.1
Rotor core outer surface	1551.3	1516.2	1549.2	1522.5
Rotor core end surface	626	843.5	950.5	1083.1
Rotor AVH surface	6583.5	6545.2	6537	6506.5
Rotor bar surface	711.1	682.9	711.3	672.7
Rotor end ring surface	2136.5	2132.2	2017.8	1960
Shaft surface	192.6	198	182.6	190.7

better improved, and vortices in the end region of the DE side are reduced. The maximum temperature rise of the rotor region decreased by 1.3%. Only focusing on the cooling enhancement effect of a single region, the installation on both sides is weaker than on one side alone. However, installing on both sides can achieve better overall cooling.

In the future study, the heat dissipation capacity will be further improved by optimizing the geometric parameters of AVGV. And reveal the matching mechanism when installed on both sides together.

Author statement

Ziyi Xu: Formal analysis, Investigation, Writing - Original Draft, Visualization.
Yongming Xu: Funding acquisition, Conceptualization, Methodology, Supervision.
Wenhui Liu: Validation, Resources.
Yaodong Wang: Software, Data Curation.

Declaration of competing interest

The authors declare that they have no known competing financial interests or personal relationships that could have appeared to influence the work reported in this paper.

Data availability

The authors do not have permission to share data.

Acknowledgments

This work was supported by the National Natural Science Foundation of China, under Grants (52077047).

References

[1] J. Wu, J. Hu, A. Chen, P. Mei, X. Zhou, Z. Chen, Numerical analysis of temperature distribution of motor-refrigerant in a r32 rotary compressor, Appl. Therm. Eng. 95 (2016) 365–373.
[2] W. Tong, S. Wu, R. Tang, Research on the airflow and thermal performance in a large forced air-cooled permanent magnet synchronous machine, IEEE Access 7 (2019) 162 343–162 352.
[3] N. Arbab, W. Wang, C. Lin, J. Hearron, B. Fahimi, Thermal modeling and analysis of a double-stator switched reluctance motor, IEEE Trans. Energy Convers. 30 (3) (Sept. 2015) 1209–1217.
[4] X. Fan, R. Qu, J. Li, D. Li, B. Zhang, C. Wang, Ventilation and thermal improvement of radial forced air-cooled fscw permanent magnet synchronous wind generators, IEEE Trans. Ind. Appl. 53 (4) (July/Aug. 2017) 3447–3456.
[5] A. Fawzal, R. Cirstea, T. Woolmer, M. Dickison, M. Blundell, K. Gyftakis, Air inlet/outlet arrangement for rotor cooling application of axial flux pm machines, Appl. Therm. Eng. 130 (2018) 1520–1529.
[6] M.A. Mueller, et al., Improving the thermal performance of rotary and linear air-cored permanent magnet machines for direct drive wind and wave energy applications, IEEE Trans. Energy Convers. 34 (2) (Jun. 2019) 773–781.
[7] W. Chen, Y. Ju, D. Yan, L. Guo, Q. Geng, T. Shi, Design and optimization of dual-cycled cooling structure for fully-enclosed permanent magnet motor, Appl. Therm. Eng. 152 (2019) 338–349.
[8] A. Acquaviva, O. Wallmark, E.A. Grunditz, S.T. Lundmark, T. Thiringer, Computationally efficient modeling of electrical machines with cooling jacket, IEEE Trans. Transport. Electrific. 5 (3) (Sept. 2019) 618–629.
[9] Q. Chen, H. Shao, J. Huang, H. Sun, J. Xie, Analysis of temperature field and water cooling of outer rotor in-wheel motor for electric vehicle, IEEE Access 7 (2019) 140 142–140 151.
[10] W. Li, X. Zhang, S. Cheng, J. Cao, Thermal optimization for a hspmg used for distributed generation systems, IEEE Trans. Ind. Electron. 60 (2) (Feb. 2013) 474–482.
[11] X. Zhang, W. Li, B. Kou, et al., Electrothermal combined optimization on notch in air-cooled high-speed permanent-magnet generator, IEEE Trans. Magn. 51 (1) (Jan. 2015) 1–10.
[12] Y. Jiang, D. Wang, J. Chen, Q. Zhang, T. Xuan, Electromagnetic-thermal-fluidic analysis of permanent magnet synchronous machine by bidirectional method, IEEE Trans. Magn. 54 (3) (Mar. 2018) 1–5.
[13] C. Kim, K.-S. Lee, S.-J. Yook, Effect of air-gap fans on cooling of windings in a large-capacity, high-speed induction motor, Appl. Therm. Eng. 100 (2016) 658–667.

[14] Y. Gai, et al., Numerical and experimental calculation of chtc in an oil-based shaft cooling system for a high-speed high-power pmsm, IEEE Trans. Ind. Electron. 67 (6) (Jun. 2020) 4371–4380.
[15] M.H. Park, S.C. Kim, Thermal characteristics and effects of oil spray cooling on in-wheel motors in electric vehicles, Appl. Therm. Eng. 152 (2019) 582–593.
[16] B. Assaad, K. Mikati, T. Tran, E. Negre, Experimental study of oil cooled induction motor for hybrid and electric vehicles, in: Proc. Int. Conf. Elect. Mach., 2018, pp. 1195–1200.
[17] M. Jaeger, A. Ruf, K. Hameyer, T.G.-v. Tongeln, Thermal analysis of an electrical traction motor with an air cooled rotor, in: Proc. IEEE Transp. Electrific. Conf. Expo, 2018, pp. 467–470.
[18] A.F. Akawung, Y. Fujimoto, Design and thermal analysis of cooling system for high-power density motor based on airflow, in: Proc. IEEE Int. Symp. Ind. Electron., 2019, pp. 273–278.
[19] P.H. Connor, S.J. Pickering, C. Gerada, C.N. Eastwick, C. Mi- callef, Cfd modelling of an entire synchronous generator for improved thermal management, in: Proc. IET Int. Conf. Power Electron., Mach. Drives, 2012, pp. 1–6.
[20] E. Galloni, P. Parisi, F. Marignetti, G. Volpe, Cfd analyses of a radial fan for electric motor cooling, Therm. Sci. Eng. Prog. 8 (2018) 470–476.
[21] G. Singh, M. Matuonto, K. Sundaram, Impact of imbalanced wind turbine generator cooling on reliability, in: Proc. Int. Renewable Energy Congr., 2019, pp. 1–6.
[22] S. Moon, S. Lee, High-reliable temperature prediction considering stray load loss for large induction machine, IEEE Trans. Magn. 55 (6) (Jun. 2019) 1–5.
[23] N. Wang, P. Lu, X. Chang, L. Zhang, Preliminary investigation on unstructured mesh generation technique based on advancing front method and machine learning methods, Chin. J. Theor. Appl. Mech. 53 (3) (2021) 740–751.
[24] G. Liu, M. Liu, Y. Zhang, H. Wang, C. Gerada, High-speed permanent magnet synchronous motor iron loss calculation method considering multi-physics factors, IEEE Trans. Ind. Electron. 67 (7) (Aug. 2020) 5360–5368.
[25] A. Al-Timimy, et al., Design and losses analysis of a high power density machine for flooded pump applications, IEEE Trans. Ind. Appl. 54 (4) (July/Aug. 2018) 3260–3270.